Journal of The Electrochemical Society

OPEN ACCESS

Chemo-Mechanical Effects of Stack Pressure and Temperature on Anode-Free Lithium Metal Batteries

To cite this article: Wesley Chang *et al* 2022 *J. Electrochem. Soc.* **169** 090530

Journal of The Electrochemical Society, 2022 **169** 090530

Chemo-Mechanical Effects of Stack Pressure and Temperature on Anode-Free Lithium Metal Batteries

Wesley Chang,[1,2] Tongwei Xu,[1] and Daniel Steingart[1,2,3,z]

[1]*Department of Chemical Engineering, Columbia University, New York, NY 10027, United States of America*
[2]*Columbia Electrochemical Energy Center, Columbia University, New York, NY 10027, United States of America*
[3]*Department of Earth and Environmental Engineering, New York, NY 10027, United States of America*

Electrochemical cells using rechargeable lithium metal anodes are sensitive to operating temperature and stack pressure. Current understanding generally assumes that temperature drives changes in lithium metal surface chemistry while stack pressure impacts the anode morphology. In this study, we provide quantifiable evidence for these assumptions and propose mechanisms to guide understanding of temperature and pressure effects on lithium metal cell dynamics. Beyond the direct coupling of pressure with mechanics and temperature with kinetics, we also explore possible effects of temperature on cell mechanics and stack pressure on cell chemistry. We investigate an electrolyte composition based on LiDFOB salt, using a range of operando and ex situ techniques. Mechanistic mapping of temperature- and pressure-dependent cell behavior will aid development of improved lithium metal batteries.

 [DOI: 10.1149/1945-7111/ac91a9]

Manuscript submitted June 24, 2022; revised manuscript received August 16, 2022. Published September 29, 2022.

Higher energy density batteries will further the market penetration of electric vehicles by increasing range and decreasing cost.[1] Lithium metal batteries in the anode-free configuration with zero excess lithium enable cell-level energy densities up to 60% higher than a lithium-ion cell.[2,3] Loss of electrochemically active lithium due to irreversible electrolyte degradation reactions hinders the development of an anode-free lithium metal battery and implies the need for more compatible electrolytes for lithium metal. The lower susceptibility of lithium trifluoromethanesulfonate (LiTFSI) or lithium difluoro(oxalato)borate (LiDFOB) salt electrolytes to hydrolysis in comparison with lithium hexafluorophosphate ($LiPF_6$) enables greater compatibility with lithium metal anodes. For instance, Weber et al. demonstrated improvements in anode-free cycle life from less than 20 cycles to over 80 cycles by replacing $LiPF_6$ with LiDFOB salt at a standard one molar concentration in carbonate solvents.[4] Previous work by Schedlbauer et al. and Lucht et al. proposed that oligomeric decomposition of LiDFOB forms an elastic solid-electrolyte-interphase (SEI) along with uniformly distributed LiF embedded in the SEI.[5,6] Subsequent work by Louli et al. optimized dual-salt combinations of LiDFOB with lithium tetrafluoroborate ($LiBF_4$) with anode-free cycle life approaching 200 cycles at a C/5 charge rate.[2] The current cycle life of anode-free lithium metal batteries is still far from commercial electric vehicle adoption, but the anode-free form factor is useful for rapidly iterating across different electrolytes in ongoing research and development.

Many studies on anode-free cells operate under higher stack pressures or operating temperatures than that applied to commercial lithium-ion cells. A higher stack pressure, defined as compressive force in the uniaxial direction, improves interfacial contact. A higher operating temperature increases lithium diffusion and charge transfer rates. While stack pressure in lithium-ion pouch cells is no higher than 250 kPa,[7] Weber et al. and Louli et al. utilized stack pressures to over 2 MPa for anode-free lithium metal cells in order to mechanically constrain deposited lithium on copper.[2,4,8] The LiDFOB-based electrolytes are promising alternatives to $LiPF_6$ for lithium metal batteries, but given the range of reported operating conditions in the literature, a complete chemo-mechanical study of various stack pressure and operating temperature regimes will be helpful in engineering optimal operating conditions.

Here, we conduct studies on anode-free lithium metal pouch cells to decouple the effects of stack pressure and temperature on cell performance:

(1) Quantitative morphological analysis determines the relationship between characteristic particle length scales and operating conditions.
(2) Operando acoustic transmission detects physical changes within the cell as a function of operating condition, including non-uniform deposition and cell gas formation.
(3) Anode and cathode effects on operando acoustic transmission are decoupled by investigating Li/Cu cells to study metal plating dynamics, including interfacial contact, surface chemistry, cell impedance and electrochemical kinetic measurements.

These experiments are conducted with LiDFOB salt in diethyl carbonate (DEC) and fluoroethylene carbonate (FEC) solvents (at one mole salt per liter solvent concentration). Acoustic transmission, previously demonstrated as an effective mechanical characterization technique for commercial lithium-ion batteries, probes physical changes in multilayered anode-free lithium metal pouch cells (single-crystal $LiNi_{0.5}Mn_{0.3}Co_{0.2}O_2$, or NMC532, cathode with Cu as the negative current collector) in operando as a function of stack pressure and temperature.[9–11] Acoustic transmission can be conducted in operando without damaging the cell, which is useful for probing macroscopic physical properties of pouch cells during cycling. Previously, operando acoustic transmission has been used to characterize lithium-ion cell behavior including gas formation detection, lithium plating quantification, and cell stiffness measurements from sound speed and thickness changes.[10–12] 2D operando acoustic scanning has also been developed to visualize spatial heterogeneities across the pouch cell.[13] Most recently, acoustic transmission has been applied to lithium metal cells including electrolyte dry out and solid-state battery interfacial contact loss.[2,14] Acoustic transmission involves the passage of sound waves at ultrasound frequencies (~1 to 10 MHz), where each interface between two materials results in a partial reflection and partial transmission of the wave. The reflection coefficient at each interface is a function of the acoustic impedance, which is the product of the density and sound speed through the given material.

If the interface is imperfect, then acoustic waves will pass through the contacted regions and reflect/disperse at the gaps. The effect of acoustics on imperfect solid-solid contacts has been explored in other fields and similar relations can be applied to

[z]E-mail: dan.steingart@columbia.edu

battery materials. Biwa et al. proposed a non-linear contact model, where growth asperities at the interface support the load (stack pressure).[15] Under load, these growth asperities will flatten (plastically deform), resulting in a change in the interfacial contact and a measurable difference in the transmitted acoustic amplitude. Biwa et al. treat this interface as a spring interface with an "interfacial stiffness," and determine a power law relationship between the stack pressure and the degree of contact. Dwyer-Joyce et al. further point out that this interfacial stiffness obtained from acoustic measurements is not related to the real area of contact, because spherical sound waves will pass through the imperfect interface in a non-linear manner.[16] They show that the interfacial stiffness is primarily dependent on the width and spacing of the interface gaps. While these studies were primarily theoretical and focused on general solid-solid contacts, they can be readily applied to lithium metal cell interfaces, where non-uniform deposition and stripping of lithium metal within the pouch cell acts as an acoustic scatterer. The constant pressure acoustic rig used in the current study is shown in Figs. 1a, and 1b shows how amplitude attenuates due to sound scattering from roughened interfaces.

As lithium metal cells begin to be made in larger multi-layered pouch cells, interfacial mechanical contact becomes more important to measure. As opposed to lithium-ion cells where bulk electrode phase changes dominate the thickness and stress evolution of the cell,[8] a lithium metal anode involves plating and stripping of metal without phase change. The surface roughening during non-uniform deposition scatters the ultrasound wave, causing attenuation of the transmitted wave intensity.[15,17] This wave dispersion effect due to growth asperities at a material interface is well known in acoustic non-destructive testing in other fields.

Taken together, our results in this study bring new insight into how operating conditions of stack pressure and temperature result in significant changes to cell mechanics, chemistry, and electrochemistry (and by extension, the evolution of morphology and cycling behavior during lithium plating and stripping). Understanding these dynamic and interrelated changes will aid in the development of improved anode-free lithium metal batteries, which likely require a combination of enhanced mechanical stability and an electrolyte composition with optimal chemical and electrochemical stability.

Experimental

Multi-layered pouch cells.—Machine-made multilayered pouch cells of ~200 mAh nominal capacity were purchased dry from Li-Fun Tech. The cells consist of single-crystal $LiNi_{0.5}Mn_{0.3}Co_{0.2}O_2$, or NMC532 (18.78 g cm^{-2} coating density, 3.3 g ml^{-1} density, 94:4:2% active material:carbon:binder weight ratio) and copper metal foil. Pouch cells were injected with 0.6 ml electrolyte prior to vacuum sealing (5 s at 200 °C top and 160 °C bottom seal temperature). Pouch cells were left for at least 48 h prior to cycling to allow for complete electrode wetting. Constant current cycling was conducted between 3.0 and 4.2 V, with C/3 rate equivalent to 66 mA (roughly 0.7 mA cm^{-2}).

Single-layer pouch cells.—Lithium metal - copper pouch cells were fabricated in an Argon-filled glovebox. Lithium metal and copper foils were cut into 2 cm by 2 cm pieces. Copper foil (Goodfellow, 99.95% purity, 6 μm thick) was rinsed in 10% w/v oxalic acid to remove the native oxide layer, then rinsed in deionized water and dried with a Kimwipe before transferring into the glovebox. 50 μl electrolyte was pipetted onto the copper foil, followed by a Celgard separator wound between copper and lithium foils, and another 50 μl of electrolyte was pipetted onto the lithium foil side. Nickel tabs were placed on the back sides of the lithium and copper foils. The pouch was sealed with a heat impulse sealer. Electrolyte salts were obtained from Sigma-Aldrich and dried at 150 °C under vacuum before mixing with solvents (FEC from Alfa Aesar, 98%, DEC from Sigma-Aldrich) to obtain the desired electrolyte composition. A current density of 0.5 mA cm^{-2} (2 mA over 4 cm^2) was applied during plating/stripping tests.

Acoustic transmission.—Constant stack pressure tests were conducted in a custom-made pressure rig with pressure applied pneumatically with a double piston hydraulic cylinder (Fig. 1a). Acoustic transducers (Olympus, 2.25 MHz central frequency) were placed in-line, along with low acoustic attenuation spacers made of cross-linked polystyrene (Rexolite). An ultrasonic pulser (Compact Pulser) was connected to the transmitting transducer, and a high resolution oscilloscope (Picoscope) sampling at 1 GS s^{-1} was connected to the receiving transducer. Typically, a pulse width of 2.25 MHz was applied to the pulser and read by the oscilloscope every 1–2 s. Total amplitude is calculated from the total transmitted wave intensity.

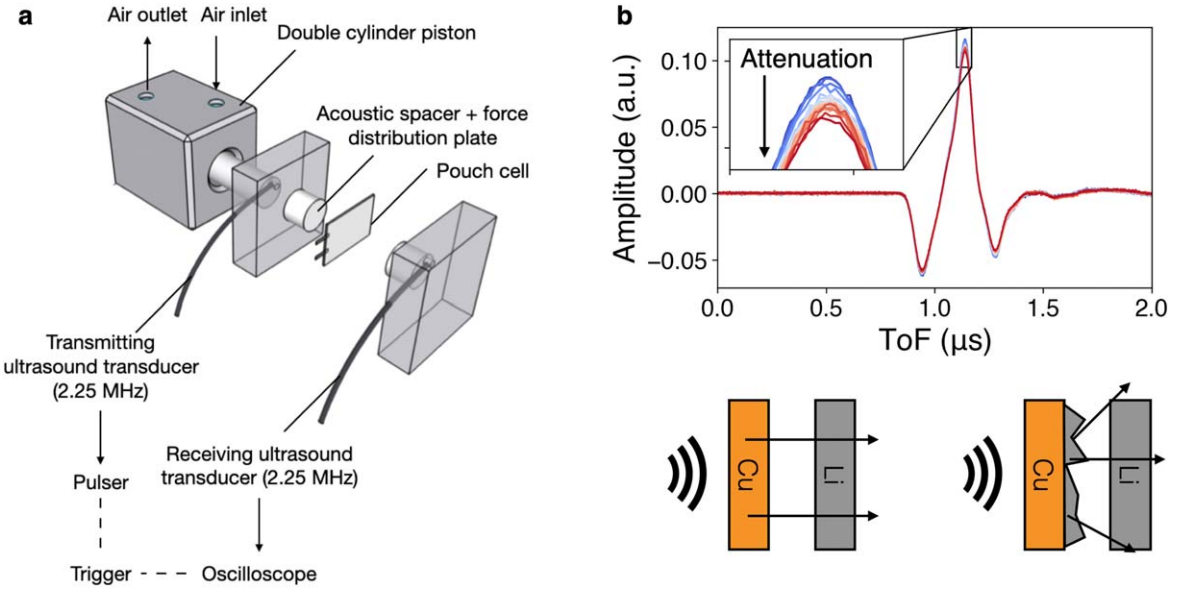

Figure 1. (a) Schematic of constant pressure holder for operando acoustic transmission tests of pouch cells. (b) Example waveforms showing attenuation of transmitted amplitude after non-uniform lithium deposition on copper, with schematic indicating physical origins of wave attenuation through a roughened interface.

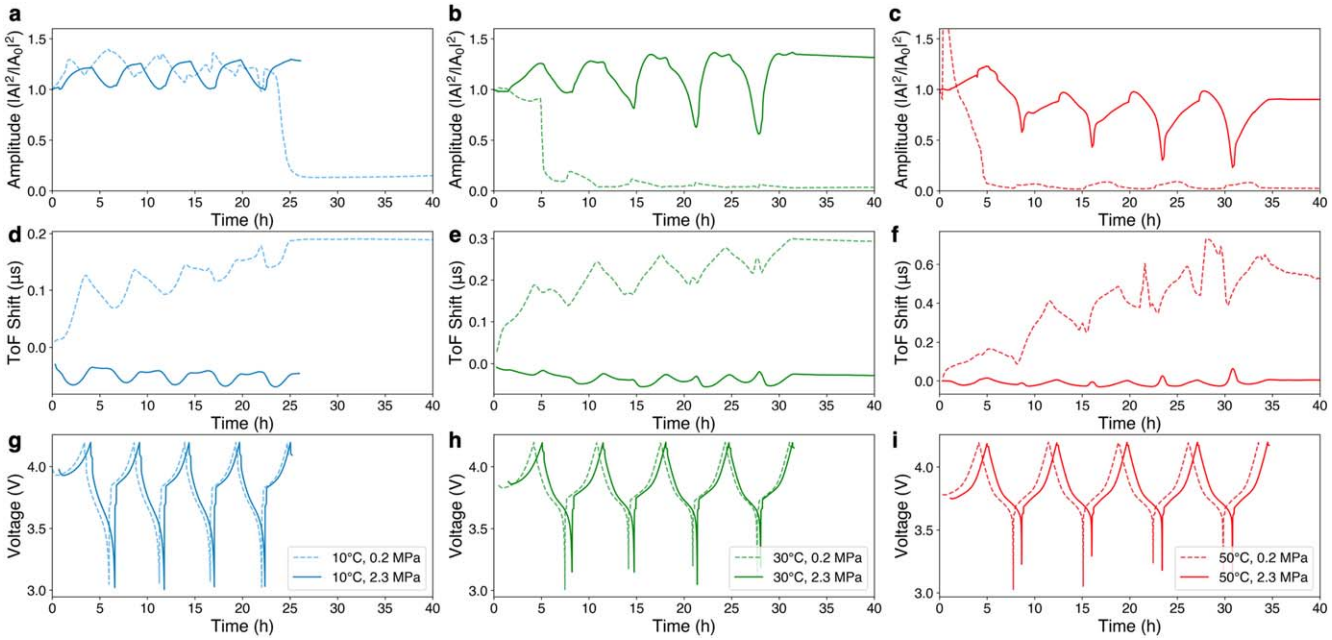

Figure 2. Operando acoustic transmission amplitude at (a) 10 °C, (b) 30 °C, and (c) 50 °C, corresponding time-of-flight shift measurements at (d) 10 °C, (e) 30 °C, and (f) 50 °C, and cycling voltage profiles at (e) 10 °C, (f) 30 °C, and (g) 50 °C. Dashed lines indicate a low stack pressure test at 0.2 MPa and solid lines indicate a high stack pressure test at 2.3 MPa.

Surface chemistry and electron microscopy.—X-ray photoelectron spectroscopy (PHI Versaprobe, Al source) was used to characterize the surface chemistry of the lithium metal plated copper foil after cycling. Samples were rinsed in DEC solvent and dried under vacuum prior to characterization. Samples were transferred to the XPS in inert atmosphere containers, and loaded into the XPS sample chamber while Argon was purged out. 3 to 5 averaged scans were taken for F 1 s, O 1 s, C 1 s, Li 1 s and B 1 s. A Shirley background subtraction was used, and peaks were referenced to the adventitious carbon peak at 248.6 eV. For SEM imaging, samples were rinsed in DEC and dried under vacuum, with ∼10 s of exposure to air while loading into the SEM (Zeiss Sigma VP). Images were collected with an accelerating voltage of 3 to 5 kV and a working distance of ∼4 mm. Particle size distribution analysis was done using the Python OpenCV library. Statistical analysis was conducted by random selection of 100 particles in each sample, and resampling 10,000 times to obtain statistically significant normal distributions of average particle size.

Electroanalytical techniques.—Constant current tests were conducted with a Keithley 2400 Source Measurement Unit and a four-wire connection. Electrochemical impedance spectroscopy was conducted with a Gamry 3000 potentiostat, with typical frequency range between 100000 Hz and 0.5 Hz at 14 points per decade in galvanostatic mode. EIS equivalent circuit fitting was done with the impedance.py Python package, where the ohmic resistance is determined by the intersection of the real impedance value with the x-axis, and the charge transfer resistances are determined by the Nyquist semicircle diameters. Cyclic voltammetry was conducted with three-electrode pouch cells, fabricated in a similar manner to the larger pouch cells. Potential was swept from 0 V to −0.25 V to 0.4 V vs Li^+/Li several times until a reversible potential sweep was obtained, and subsequent scans at 20 mV s^{-1} were used for comparisons at different operating conditions. To remove the effects of large overpotentials, a mask was placed in between the lithium and copper electrodes with a small 0.5 mm pinhole. The pouch bag material was used as a mask for its chemical stability to the liquid electrolyte; a 0.5 mm die was used to punch a small hole. Lithium foil (40 μm) was inserted between the separator and the mask to serve as a reference electrode. Tabs were carefully attached to each electrode with Kapton tape. The cell stack was assembled, and the pouch cell was placed in a pneumatic pressure rig contained within a temperature chamber.

Stack pressure calculations.—Cell stack pressure was determined as follows: the hydraulic cylinders apply pressure through compressed air. An in-line electronic pressure gauge measures the pressure, which is converted into applied force by multiplying by the cylinder bore area. For example, a gauge pressure of 4.4 psi and a bore radius of 1.5 inches results in an applied force of 138 N. The force is then divided by the total area under compression (see schematic in Fig. 1a, the force distributing plate). The cell stack sits in between compression plates. 138 N of applied force and a total compressed area of 4 cm^2 results in a cell stack pressure of 0.35 MPa.

Results and Discussion

Anode-free lithium metal pouch cells.—The mechanics of a lithium metal cell involve changes to metal plating morphology, cell thickness, and cathode modulus from phase transitions. The thickness and modulus changes within each electrode result in a net change in cell stiffness throughout charge and discharge. Characterizing multilayered machine-made pouch cells captures all these changes within a commercial form factor. The operando acoustic transmission data for six operating pressure and temperature conditions (low stack pressure of 0.2 MPa, high stack pressure of 2.3 MPa, and temperatures of 10 °C, 30 °C, and 50 °C) is depicted in Fig. 2. The effect of stack pressure on acoustic signals is evident. At 2.3 MPa for all three temperature conditions, the time-of-flight at a given state-of-charge does not shift over five cycles, indicative of a constant sound speed. The amplitude does not attenuate at 10 °C and 30 °C, with a roughly 10% attenuation factor at 50 °C attributed to some gas formation that is also visibly observed after removal from the pressure assembly.

On the other hand, the low stack pressure of 0.2 MPa leads to near complete amplitude attenuation for all three temperature conditions. Poorly contacting interfaces at 0.2 MPa lead to sound wave scattering, such that the wave amplitude is not transmitted through the cell. These poorly contacting interfaces at 0.2 MPa are

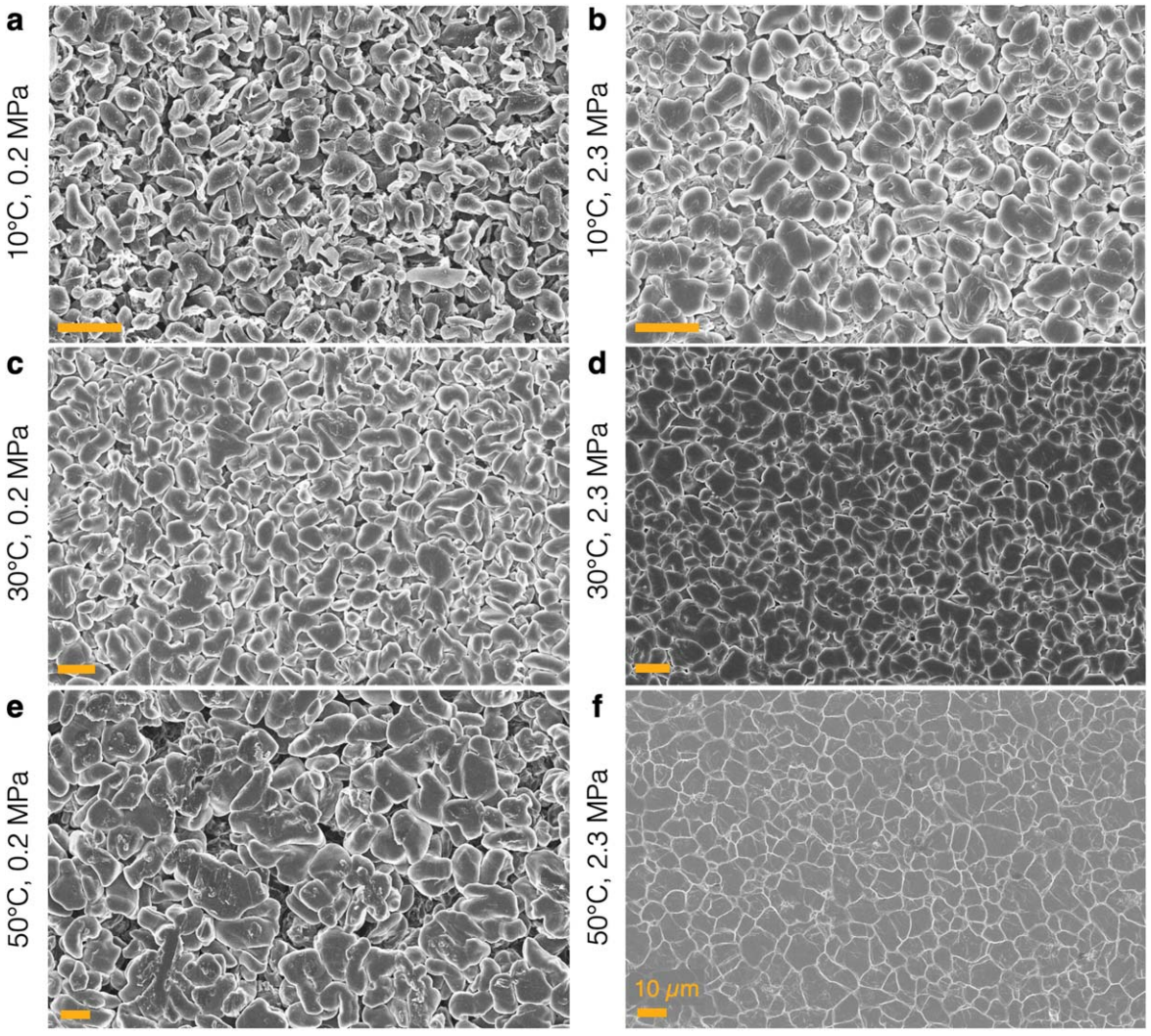

Figure 3. Lithium deposition morphology of fully charged cell (4.2 V, NMC532/Cu) at (a) 0.2 MPa and 10 °C, (b) 2.3 MPa and 10 °C, (c) 0.2 MPa and 10 °C, (d) 2.3 MPa and 30 °C, (e) 0.2 MPa and 50 °C, and (f) 2.3 MPa and 50 °C. All scale bars correspond to 10 μm.

due to a combination of surface roughness from non-uniform morphology and gas formation that does not get readily expelled from the cell stack. The amplitude attenuation is accompanied by significant increases in the wave propagation time, or the time-of-flight shift, of at least 200 ns. The time-of-flight shift indicates greater cell expansion and lower sound speeds. These observed acoustic effects of metal interfaces differ from lithium-ion cell ultrasound signals, which are dominated by graphite intercalation mechanics.

To correlate the operando acoustic transmission data with lithium morphology, quantitative particle analysis is conducted from ex situ SEM images after charging on the fifth cycle (Fig. 3). The SEM images show that 2.3 MPa stack pressure results in dense plating in all three temperature conditions (Figs. 3b, 3d, 3f), and 0.2 MPa results in porous plating in all three temperature conditions (Figs. 3a, 3c, 3e). Average particle sizes from statistical resampling are positively correlated with temperature. A low stack pressure of 0.2 MPa and low temperature of 10 °C results in an average particle size of 2.7 μm^2 (Fig. 4a), which increases to 16.1 μm^2 at 0.2 MPa and 30 °C (Fig. 4b), and to 35.2 μm^2 at 0.2 MPa and 50 °C (Fig. 4c). A higher stack pressure of 2.3 MPa results in an increase of average particle size to 5.8 μm^2 at 10 °C (Fig. 4a), an increase to 22.4 μm^2 at 30 °C (Fig. 4b), and an increase to 53.5 μm^2 at 50 °C (Fig. 4c). Elevated temperature increases the average particle size due to lower surface energy favoring growth-dominated plating over nucleation-dominated deposition. Higher compression forces than the yield stress of lithium metal (~0.8 to 1 MPa)[18] lead to creep and reduced layer porosity.

As described, physical changes of the cell such as lithium morphology, cell expansion and gas formation are detectable by operando acoustic transmission. Amplitude attenuation is correlated with poor contact, such as porous deposits at low stack pressures. The time-of-flight shift is directly related to overall cell expansion, since the sound speed is a function of cell stiffness and thickness. In lithium metal batteries, these physical changes are also linked to surface chemistry, since non-uniform deposits are expected to correlate with increased electrolyte decomposition. To understand these chemo-mechanical relationships of lithium metal batteries, XPS is conducted for each of the six lithium metal films after the fifth full charge to 4.2 V (Fig. 5). The F 1 s scans show increased salt decomposition product, $LiBF_4$, for cycling at 50 °C. This species, associated with the fitted peak at 689 eV, comprises 68 wt% and 91 wt% in the 50 °C cells (Figs. 5i, 5k), but less than 50 wt% in the lower temperature cells (Figs. 5a, 5c, 5e, 5g). Previous work indicates that $LiBF_4$ is a primary decomposition product formed from LiDFOB.[19–21] High operating temperatures are expected to increase the rate of this decomposition reaction, resulting in more $LiBF_4$ in the SEI. The other fitted peak at 687 eV is assigned to LiF, another common SEI product. Aside from the temperature dependence, $LiBF_4$ and LiF also indicate some dependence on stack

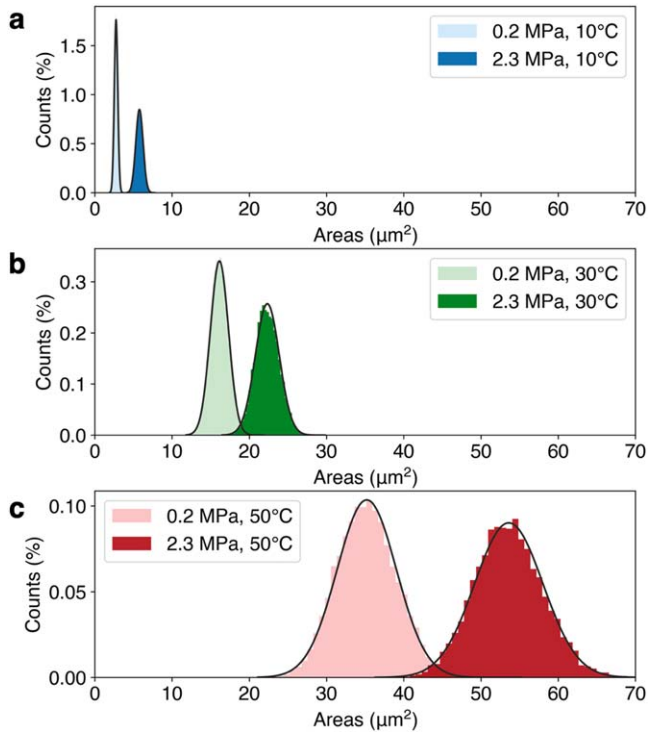

Figure 4. Quantitative microstructure analysis of lithium deposits in fully charged cells (4.2 V), for (a) 10 °C, (b) 30 °C, and (c) 50 °C, each at two different stack pressures. Statistical resampling of the datasets results in normal distributions of average particle size, indicating larger average particles with increasing temperature and stack pressure.

pressure. For all three temperature conditions, there is less $LiBF_4$ and more LiF at the higher stack pressure of 2.3 MPa. The compact deposits at higher stack pressure are correlated with less salt decomposition to $LiBF_4$ and increased LiF generation. These surface chemical species agree with commonly observed SEI species for carbonate electrolytes. Carbonate decomposition products indicated by the C 1 s scan are similar for all operating conditions (Figs. 5b, 5d, 5f, 5h, 5j, 5l).

Interfacial contact and deposition morphology.—The cyclical changes in both amplitude and time-of-flight with state-of-charge indicate the relationship with cell thickness and modulus, similar to previous studies on Li-ion batteries. This is useful for lithium metal cell state estimation if machine learning methods are incorporated. However, deciphering the root cause of these signal changes can be challenging in full cells due to the coupled effects of the anode and cathode, and the effect of a multi-layered geometry. The sound propagation mechanics through thin multi-layered cells are complex, with the wave partially transmitting and reflecting through each interface. To decouple anode from cathode effects on acoustic transmission signals, single-layer Li/Cu pouch cells are constructed. A single Li/Cu layer is the simplest geometry to probe the acoustic effects of lithium deposition. The only change that occurs is between the lithium and copper layer, where the lithium is plated and stripped. Therefore, the changes in acoustic transmission can be attributed to lithium morphology changes.

The acoustic transmission results of single-layer Li/Cu cells show that a lower stack pressure of 0.35 MPa results in significant amplitude attenuation at all three temperature conditions, with ~40% attenuation at 50 °C and up to 90% attenuation at 10 °C (Fig. 6a). Measured overpotentials decrease with both increasing temperature and stack pressure (Fig. 6b). Most of the amplitude attenuation occurs during the first plating step, where lithium first nucleates on the fresh copper surface. The deposition morphology of lithium on the copper substrate after 10 cycles (after the 11th plating step) shows non-uniform growth at 0.35 MPa, with 50 °C resulting in larger particle sizes than 10 °C (Figs. 6c, 6e, 6g). On the other hand, a higher stack pressure of 2.3 MPa at any temperature results in compact and dense lithium deposits without any measurable amplitude attenuation (Figs. 6d, 6f, 6h). Instead, the acoustic amplitude steadily increases by around 10% over the course of 10 plating and stripping cycles. Since the high stack pressure condition of 2.3 MPa is above the yield stress of ~0.7 to 0.8 MPa for bulk lithium metal,[18] the lithium foil plastically deforms over time, resulting in a lower lithium thickness and a higher acoustic amplitude. The acoustic wave amplitude is inversely proportional to the thickness of the medium through which it propagates. Amplitude attenuates with increased interfacial roughness that scatters and disperses the transmitted sound wave.

Operando acoustic transmission of single-layer lithium/copper pouch cells decouples anode plating effects from cathode phase change and gassing effects. The attenuation observed at low stack pressures or low temperatures is related to poor interfacial contact, as confirmed by the non-uniform growth morphologies at the micron-scale observed in post-mortem cell disassembly and SEM. Lower stack pressure and/or lower operating temperature also results in high DC overpotentials (Fig. 6b). The sensitivity of deposition morphology with stack pressure described here is similar to recent results reported by Harrison et al. for stack pressure effects in 4 M LiFSI DME.[22] In their work, increasing stack pressure from 0 MPa to 1 MPa improves cell-to-cell reproducibility and Coulombic efficiency, but a high stack pressure of 10 MPa demonstrated evidence of soft short circuits. In the current work, further increasing stack pressure from 0.35 MPa up to 2.3 MPa continued to lower the lithium overpotential, increase the average microstructure size, and improve cycling performance.

Interfacial contact is largely a function of stack pressure, with higher stack pressure flattening lithium deposits and forcing plastic deformation of soft lithium metal (with a bulk yield stress of $<$ 1 MPa). An elevated temperature of 50 °C also results in noticeably more compact deposits than a cold temperature of 10 °C. Genovese et al. previously explored the effect of a hot formation protocol on a similar electrolyte (LiDFOB/$LiBF_4$), where two initial cycles at an elevated 40 °C resulted in a tripling of the cycle life before 80% capacity retention.[23] Chemical analysis in the present study reveals greater salt decomposition product at 50 °C in comparison with lower temperatures.

Impedance evolution during lithium plating and stripping.—To further investigate the dynamic changes of the lithium metal electrode, electrochemical impedance spectroscopy (EIS) was taken after each plating and stripping step. The EIS curves were fitted and the resulting charge transfer resistance was plotted (Fig. 7). For example, the two cells at 30 °C and 0.35 MPa, and 30 °C and 2.3 MPa are shown in Fig. 7. The low stack pressure cell measured ~40 ohms R_{ct} after each plating step (Fig. 7a) and over 50 ohms after each stripping step (Fig. 7b), with the impedance relatively stable within the 10 cycles. The high stack pressure cell measured 40 ohms R_{ct} and less after each plating step (Fig. 7c) with a more pronounced decrease over cycling because of the effects of plastic deformation at 2.3 MPa (Fig. 7c). The decrease in cell impedance suggests that plating morphology becomes more compact over multiple cycles and with a lower surface area. The R_{ct} after each stripping step increased significantly after the fourth cycle from less than 100 ohms to over 200 ohms (Fig. 7d). It is likely that efficient stripping exposes more bare copper to electrolyte, which has a high contact resistance.

Figure 8a shows the R_{ct} from all EIS tests after each plating step, when ~5 μm were deposited on copper. R_{ct} remained below 100 ohms for all cells tested. Lower cell impedance after plating is correlated with denser morphologies at higher stack pressures or higher temperatures. Figure 8b shows the R_{ct} from the EIS tests after each stripping step, where only residual electrochemically inactive lithium was left behind on the copper substrate. In each of the three

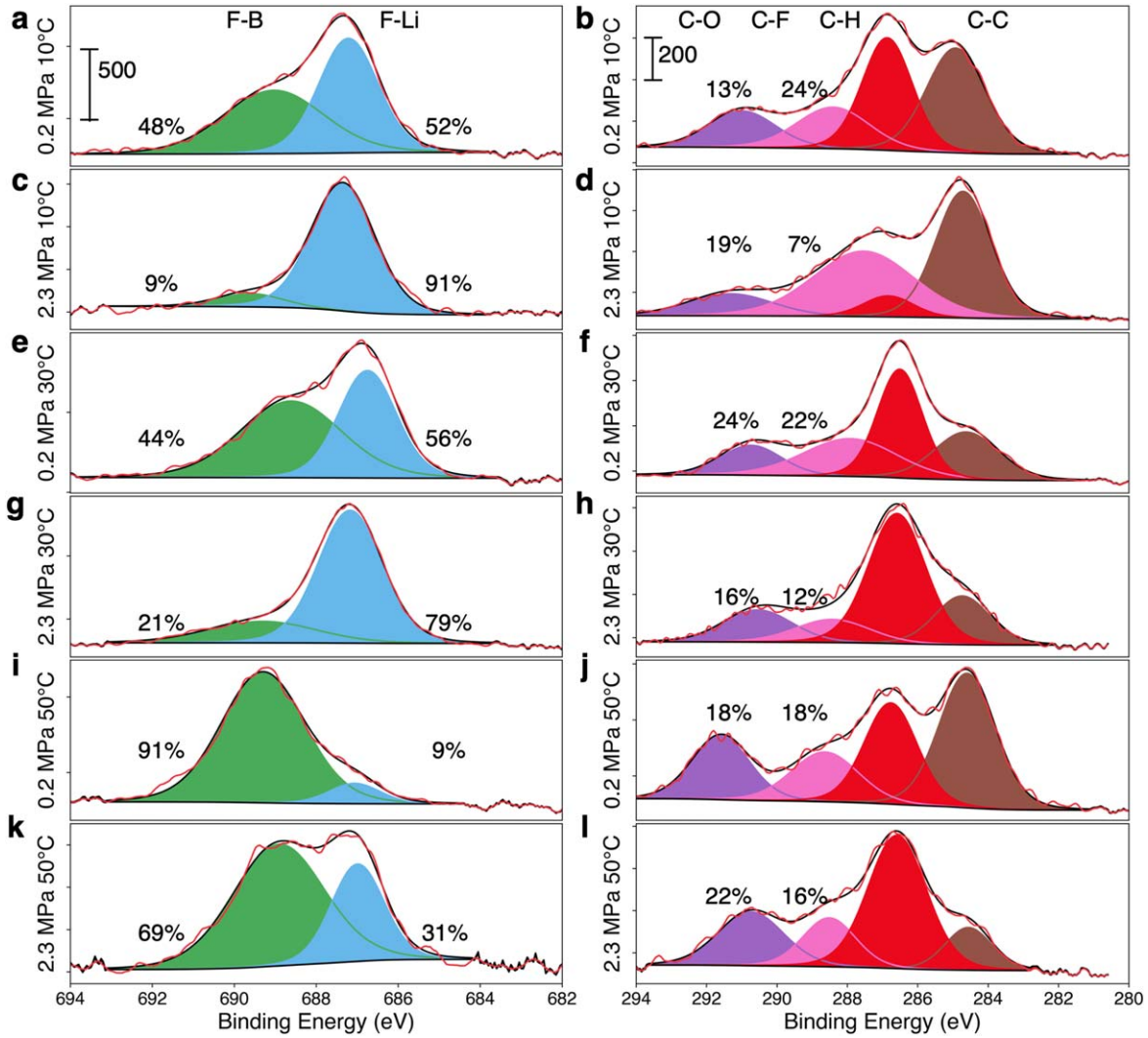

Figure 5. XPS of charged anode at 4.2 V (lithium plated on copper) with (a) F 1 s scan and (b) C 1 s scan at 0.2 MPa and 10 °C, (c) F 1 s scan and (d) C 1 s scan at 2.3 MPa and 10 °C, (e) F 1 s scan and (f) C 1 s scan at 0.2 MPa and 30 °C, (g) F 1 s scan and (h) C 1 s scan at 2.3 MPa and 30 °C, (i) F 1 s scan and (j) C 1 s scan at 0.2 MPa and 50 °C, and (k) F 1 s scan and (l) C 1 s scan at 2.3 MPa and 50 °C. Each *y*-axis tick mark for the F 1 s scans corresponds to 500 counts, and each *y*-axis tick mark for the C 1 s scans corresponds to 200 counts.

temperature conditions, the stripped electrode results in a higher measured resistance, which is attributed to the exposure of bare copper to electrolyte. The high stack pressure cases result in a higher R_{ct} than the low stack pressure cells, attributed to more efficient stripping of lithium and lithium species. Bare copper has a higher contact resistance with electrolyte than residual lithium SEI species. These results indicate that acoustic transmission provides information on cell mechanics not apparent in EIS. The more efficient deposition and stripping of lithium at high stack pressures results in improved contact, as indicated by the lack of amplitude attenuation throughout cycling; however, it also leads to higher cell impedance towards the end of stripping because of the contact resistance of bare copper.

The EIS tests at the end of each plating and stripping step reveal the evolution of cell impedance throughout multiple plating and stripping cycles. To obtain higher fidelity impedance measurements for comparison with acoustic measurements of interfacial contact, EIS was also periodically conducted within one cycle. EIS was conducted after every 0.2 mAh cm^{-2} of charge passed on the first plating and stripping cycle, for operating conditions at 30 °C and 2.3 MPa. Figure 9a depicts the voltage profile for each 0.2 mAh plating segment, progressing from cooler (unplated) to warmer (fully plated) colors. Figure 9d depicts the voltage profile for the 0.2 mAh stripping segments, progressing from warmer (fully plated) to cooler (fully stripped) colors. The color scheme indicates the amount of charge passed. During plating, the overpotential slowly increases from 75 mV to 100 mV due to progressive SEI formation. During stripping, the overpotential initially remains steady at around −75 mV before polarizing to −1 V after all the electrochemically active lithium is stripped off. EIS was taken after each of these 0.2 mAh plating and stripping segments, after a 30 min rest to reach a pseudo-equilibrium state. Figure 9b shows the corresponding EIS curves after each plating segment, with the first curve taken prior to plating (Li/Cu), as indicated by the blocking condition. The bare copper blocking electrode is indicated by the capacitive behavior of the low frequency region. After 0.2 mAh of plating, the cell transitions to a Li/Li cell, as shown by the subsequent non-blocking behavior at low frequencies. In agreement with the DC overpotentials during galvanostatic current, the charge transfer resistance, indicated by the magnitude of the semicircle, gradually increases by around 20 mV (Fig. 9c). Figure 9e shows the corresponding EIS curves after each stripping segment, where the first curve in red prior to stripping is similar to the last curve in Fig. 9b after fully plating, both indicating a charge transfer resistance of around 75 ohms. The charge transfer resistance increases significantly towards the end of stripping (Fig. 9f), in agreement

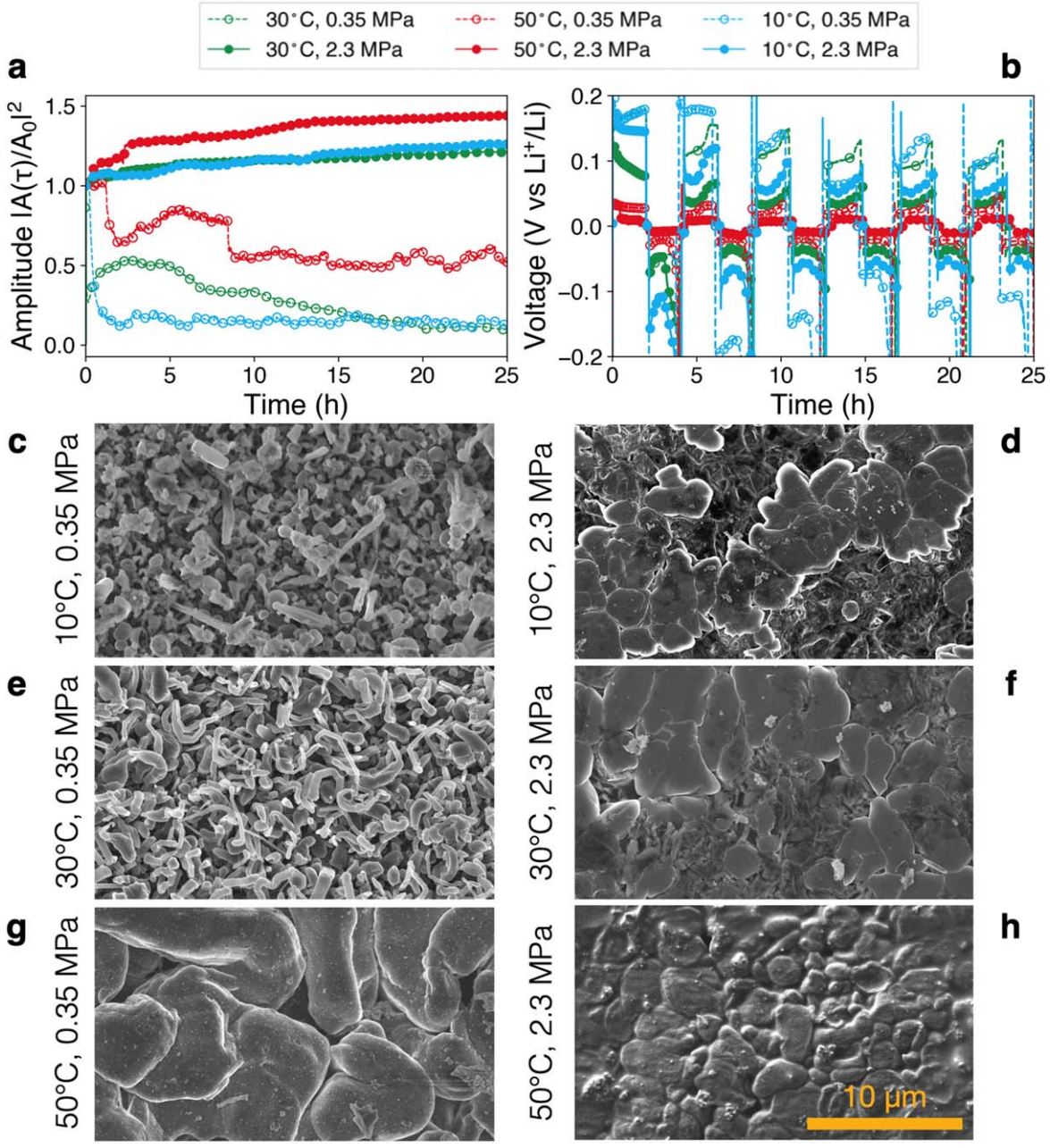

Figure 6. Interfacial contact and growth morphology at six stack pressure and temperature conditions. (a) Acoustic amplitude over 10 plating and stripping cycles in a lithium/copper pouch cell. (b) Voltage profiles for the corresponding plating and stripping cycles. SEM images of lithium deposition morphology on copper after 11 plating steps, for (c) 10 °C, 0.35 MPa, (d) 10 °C, 2.3 MPa, (e) 30 °C, 0.35 MPa, (f) 30 °C, 2.3 MPa, (g) 50 °C, 0.35 MPa, (h) 50 °C, 2.3 MPa. All images are the same magnification, with the scale bar corresponding to 10 μm.

with the DC overpotentials, where the voltage polarization is partly due to the contact resistance of bare copper. At −1 V, most of the plated lithium is stripped off the copper electrode, leaving behind trace lithium and SEI species and exposing the bare copper to electrolyte. This interface, however, is no longer an ion-blocking interface as it was in the pristine uncycled state, due to the presence of a formed interphase and remainder lithium species. In comparing this data to the acoustic amplitude, the significant attenuation event during initial plating is correlated with the significant drop in cell impedance. As lithium nucleates to form a plated layer on copper, this relatively porous and non-uniform initial layer causes wave dispersion resulting in the observed attenuation event. At the same time, the presence of plated lithium reduces the cell impedance significantly, in contrast to bare copper foil. The electrochemical measurements are interfacial by nature, whereas the acoustic transmission measurements are sensitive to macroscopic features.

Stack pressure and transient voltammetry.—We have demonstrated that cycling lithium metal in LiDFOB electrolyte at 50 °C rather than 30 °C leads to denser lithium plating morphology with higher Coulombic efficiencies, but with increased gas formation and salt decomposition products in the SEI. We complement these chemo-mechanical analyses and corresponding impedance measurements with transient voltammetric analysis. To avoid the influence of large overpotentials that are predominant in lithium/copper cells, but simultaneously enable measurements as a function of stack pressure, we design a pouch cell with a mask to reduce the total contact area (Fig. 10a).[24] A reference electrode was inserted to

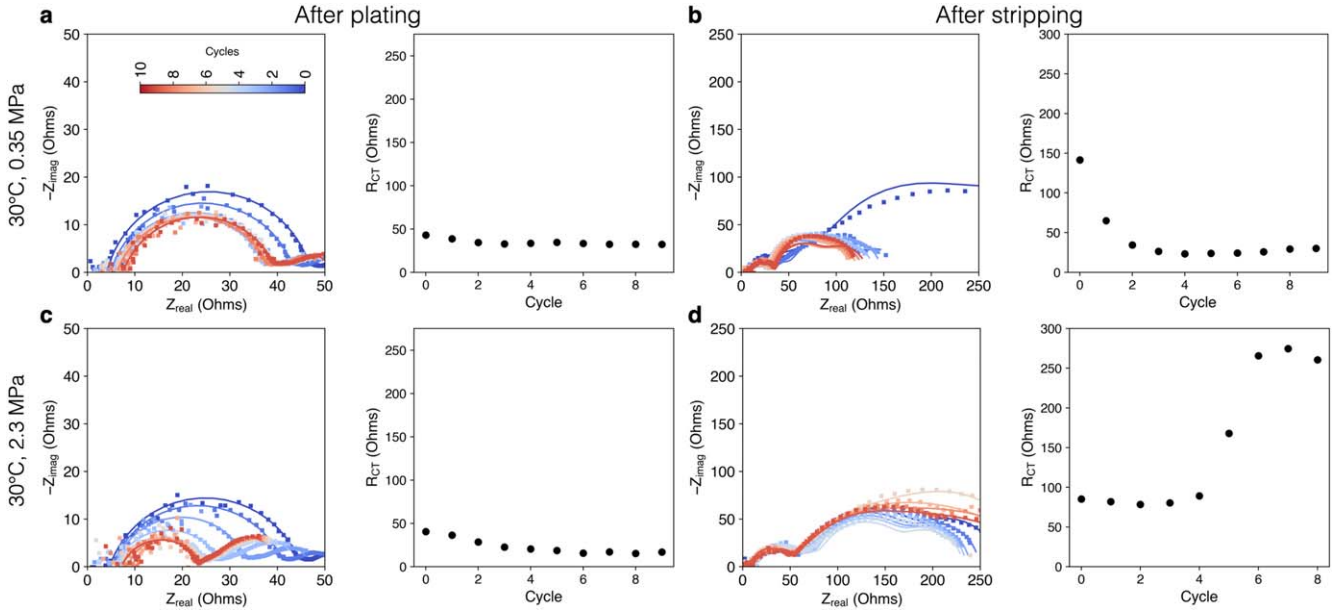

Figure 7. Electrochemical impedance spectroscopy (EIS) conducted after each (a) plating step (0.5 mA cm^{-2} for 1 mAh cm^{-2}) at 0.35 MPa and (b) stripping step at 0.35 MPa, and each (c) plating step at 2.3 MPa and (d) stripping step at 2.3 MPa, all at 30 °C. Repeated plating/stripping at the higher stack pressure results in a steady decline in cell impedance after plating because of mechanical compression and compact lithium deposition. The cell impedance after stripping is much higher because most of the lithium can be pulled off, resulting in more exposed copper.

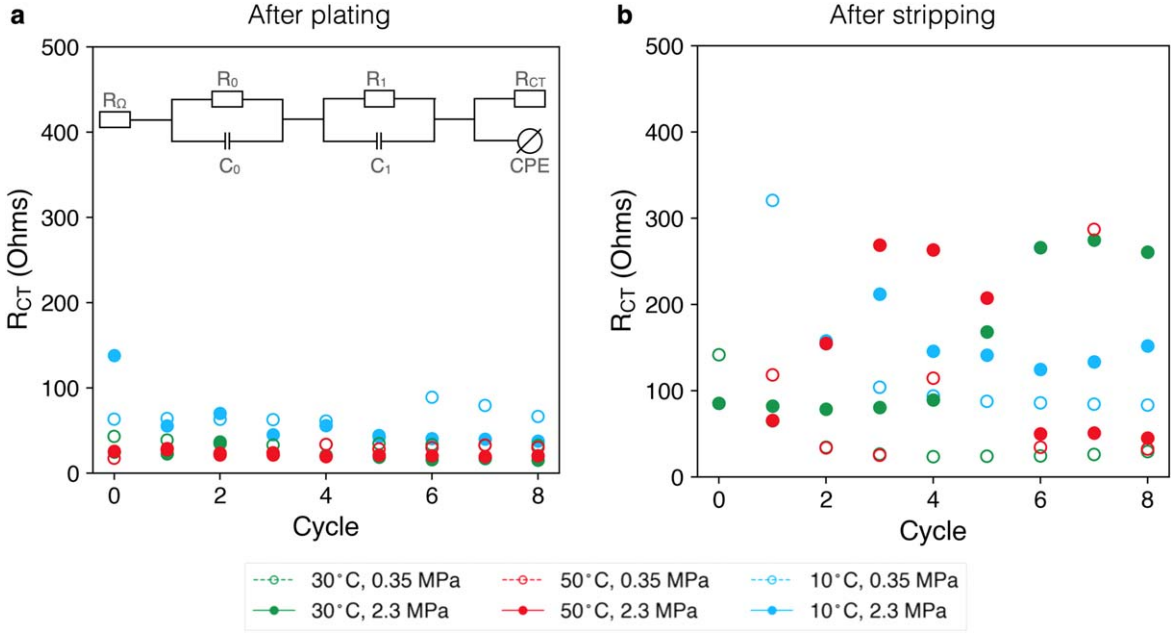

Figure 8. Electrochemical impedance spectroscopy (EIS) of all six stack pressure and temperature conditions. (a) after plating steps on copper at 0.5 mA cm^{-2} for 1 mAh cm^{-2}. (b) after stripping off copper at −0.5 mA cm^{-2} current density until −1 V vs Li^+/Li.

establish a stable reference potential during voltammetry. Our previous chemo-mechanical measurements and bulk electrochemical measurements are complemented with more precise electrochemical analysis. The cyclic voltammetry (CV) results shown in Fig. 10b indicate a significant temperature dependence, with 50 °C resulting in higher stripping peak currents than 30 °C and 10 °C. This agrees with prior work by Verbrugge et al. using microelectrodes to determine relationships between temperature and transient electrochemical response, with higher temperatures leading to higher exchange current densities.[25] While conventional microelectrodes with tungsten wires are ideal for minimizing total electrode area, it is not possible to measure these electrochemical transients as a function of stack pressure. Pouch cell geometries with small contact areas enable stack pressure measurements while minimizing overpotentials. Stack pressure does not have a measurable effect on the transient current response, and both the low and high stack pressure conditions at any given temperature result in nearly identical CV curves (Fig. 10b). This result is expected, and recent modeling work has demonstrated that the relatively low stack pressure operating regimes below 10 MPa should not significantly alter transient electrochemical properties.[26] CV tests of larger area electrodes reveal similar temperature-dependent behaviors but with more linear, ohmically-dominated curves. This small contact area pouch cell design may be useful in future studies for accurate

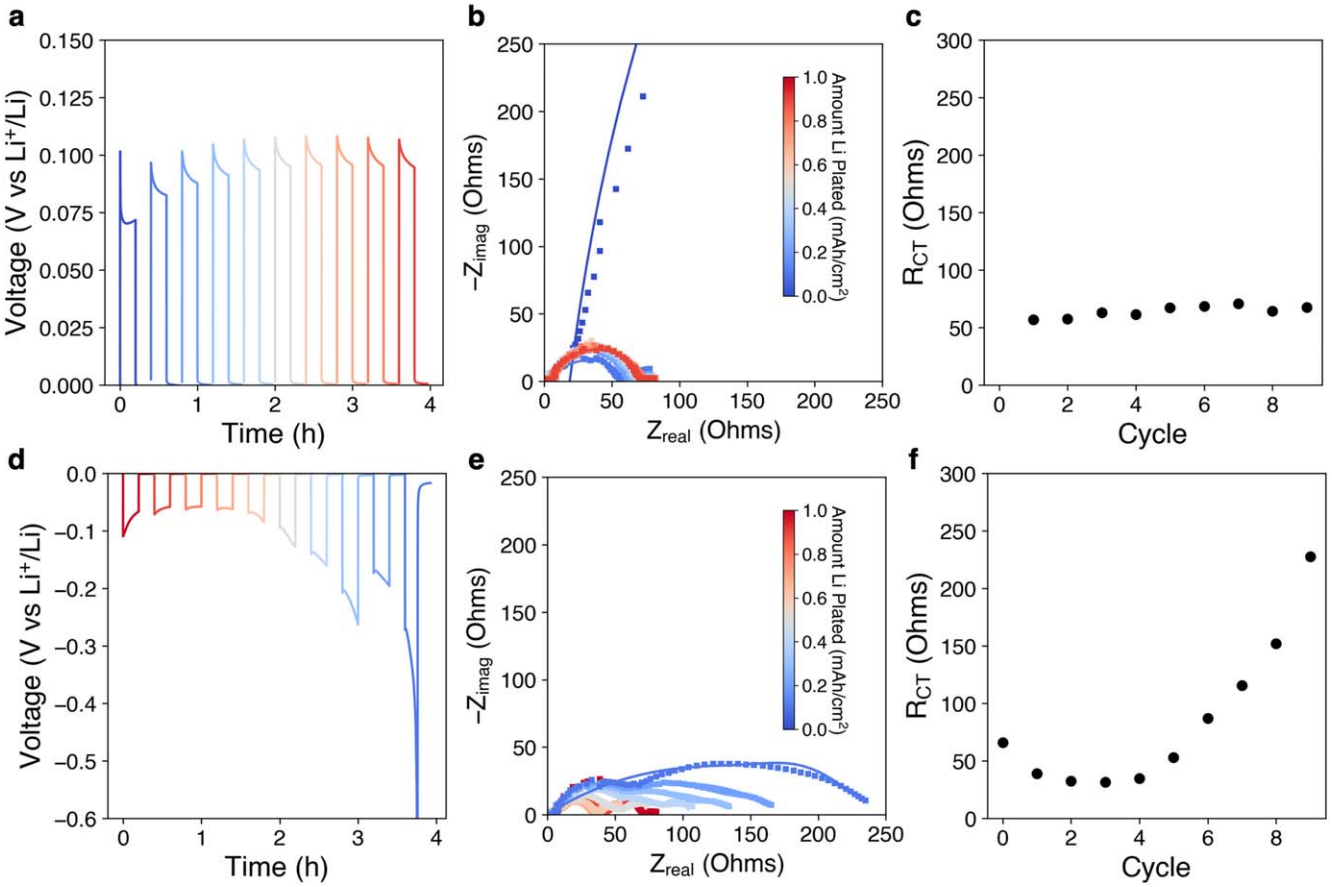

Figure 9. Electrochemical impedance spectroscopy (EIS) within a single plating/stripping cycle at intervals of 0.2 mAh cm^{-2} (current density at 0.5 mA cm^{-2}) for a total of 1 mAh cm^{-2} charge passed (at 30 °C and 2.3 MPa). (a) Corresponding voltage curves, with EIS conducted after 30 min rest after each incremental plating step, with (b) Nyquist plots and (c) charge transfer resistances. (d) Corresponding voltage curves, with EIS conducted after 30 min rest after each incremental stripping step, with (e) Nyquist plots and (f) charge transfer resistances. The color legend indicates the amount of charge passed on the copper working electrode (warmer red color indicates the presence of 1 mAh cm^{-2} plated lithium). The large cell impedance during stripping primarily occurs towards the end of discharge as the cell is polarized, due to the increased contact resistance of copper with electrolyte.

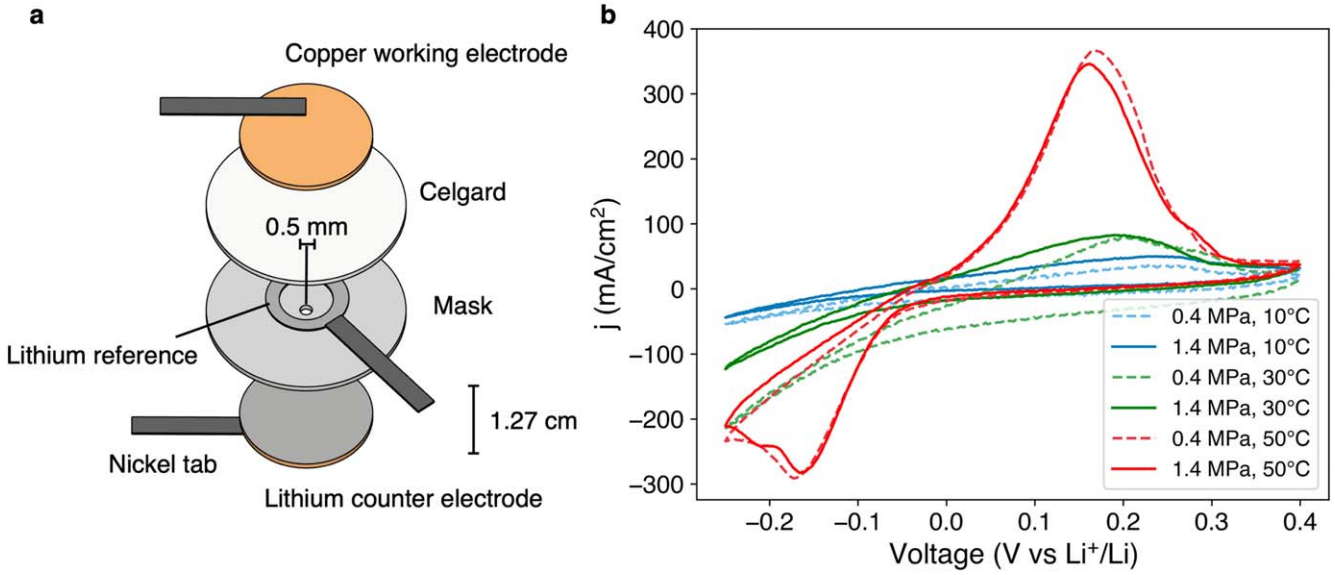

Figure 10. (a) Small contact area three-electrode pouch cell design to minimize overpotentials for transient electrochemical measurements (e.g. cyclic voltammetry). A pouch cell format allows for determination of electrochemical transients as a function of both stack pressure and temperature. Small contact area is achieved by placing a mask with a small pinhole between the separator and the lithium metal counter electrode. A lithium metal reference electrode shaped in a ring around the pinhole provides a more stable reference than using the lithium counter electrode as a reference, which changes in surface area during plating/stripping. (b) Cyclic voltammetry conducted between −0.2 V and 0.4 V vs Li^+/Li indicates an expected relationship between peak stripping current and temperature, and no relationship with stack pressure.

measurements of transient electrochemical response to stack pressure changes in liquid electrolytes. The design minimizes error from iR compensation methods. Further, the results show reproducibility, attributed to the incorporation of a geometrically uniform reference electrode ring around the center contact area.

Discussion on chemo-mechanical dynamics.—The analysis of lithium metal pouch cells with combined acoustic transmission, quantitative microstructure analysis, surface chemical analysis, electrochemical impedance spectroscopy and transient electrochemical measurements reveal complex interdependencies between cell mechanics, chemistry, and electrochemistry as a function of operating conditions. Operando acoustic transmission of multilayered NMC532/Cu pouch cells measures macroscopic cell changes as a function of pressure and temperature. A low stack pressure of 0.2 MPa is found to provide insufficient mechanical compression, leading to near complete amplitude attenuation resulting from a combination of non-uniform lithium interfaces and gas formation. 2.3 MPa at all temperature conditions results in larger lithium deposits, and can expel gas out of the cell stack. Typical lithium deposits range in size from less than 2 μm^2 at 10 °C and 0.2 MPa, to over 40 μm^2 at 50 °C and 2.3 MPa. Greater acoustic attenuation at 50 °C is attributed to increased gas formation as observed visually. On the other hand, stack pressure causes no measurable difference in surface chemistry, which is primarily affected by temperature. A temperature of 50 °C results in increased LiDFOB salt decomposition product in the SEI. To decouple the cathode and anode effects on acoustic signals, Li/Cu single-layer pouch cells are constructed as the simplest layer model for determining acoustic effects on lithium deposition. Acoustic transmission through single-layer lithium metal confirms the non-uniform lithium interface formed at low stack pressure results in immediate amplitude attenuation. Complementary EIS analysis shows that lithium metal impedance is lower during the plated, or charged, state than during the fully stripped, or discharged, state, where high contact resistance occurs with exposure of bare copper to electrolyte. Further studies using a masked electrode pouch cell with a reference electrode confirm a transient voltammetric dependence on temperature but not on stack pressure. Stack pressure changes between 0.2 MPa and 1.4 MPa do not impact electrochemical kinetics.

Overall, the lithium anode exhibits improved mechanical, chemical, and electrochemical properties with increased temperature to 50 °C and pressure to 2.3 MPa, including higher acoustic amplitude, lower cell resistance, faster peak stripping currents, and larger deposits. However, the possibility of faster gas formation and electrode cross-talk in larger full cells may lead to faster capacity fade over longer cycles. A complete understanding of lithium metal cells requires characterization of these dynamic changes and how cell non-equilibrium states can be controlled or determined during practical operation of a rechargeable lithium metal cell. Stack pressure and temperature are two critical variables which impact the morphology, chemistry, electrochemistry, and overall cell performance.

Conclusions

These findings on pressure and temperature-dependent chemo-mechanics of lithium plating and stripping in LiDFOB electrolyte will inform guidelines for operating conditions of anode-free lithium metal batteries. As more stable liquid electrolytes are introduced and larger format lithium metal cells are built, it becomes important to map out optimal operating conditions for potential commercial use cases. Regardless of electrolyte chemistry, a lithium metal anode may require higher stack pressures and operating temperatures than used in lithium-ion cells in order to stabilize anode morphology and SEI at practical rates. Using electrolytes with higher temperature stability profiles can take advantage of cell impedance reduction and faster interphase reactions, resulting in improved anode-free cell performance. To take full advantage of the high temperature or high stack pressure improvements, cathode chemistries used should also be chemo-mechanically stable at these operating conditions.

Acknowledgments

We thank generous funding from Mercedes-Benz Research and Development North America. W.C. thanks The Electrochemical Society F.M. Becket Summer Fellowship for funding part of this work. We thank productive feedback and useful discussions with Prof. Lauren Marbella and Dr Aashutosh Mistry.

Author Contributions

Conceptualization, W.C. and D.S.; Data Curation, W.C.; Methodology, W.C.; Investigation, W.C., T.X.; Writing—original draft, W.C.; Writing—review & editing, W.C., D.S.; Funding Acquisition, D.S.

ORCID

Wesley Chang https://orcid.org/0000-0002-9389-1265

References

1. J. Liu et al., *Nat. Energy*, **4**, 180 (2019).
2. A. J. Louli et al., *Nat. Energy*, **5**, 693 (2020).
3. J. Qian, B. D. Adams, J. Zheng, W. Xu, W. A. Henderson, J. Wang, M. E. Bowden, S. Xu, J. Hu, and J. G. Zhang, *Adv. Funct. Mater.*, **26**, 7094 (2016).
4. R. Weber, M. Genovese, A. J. Louli, S. Hames, C. Martin, I. G. Hill, and J. R. Dahn, *Nat. Energy*, **4**, 683 (2019).
5. S. Jurng, Z. L. Brown, J. Kim, and B. L. Lucht, *Energy Environ. Sci.*, **11**, 2600 (2018).
6. T. Schedlbauer, S. Krüger, R. Schmitz, R. W. Schmitz, C. Schreiner, H. J. Gores, S. Passerini, and M. Winter, *Electrochim. Acta*, **92**, 102 (2013).
7. A. J. Louli, J. Li, S. Trussler, C. R. Fell, and J. R. Dahn, *J. Electrochem. Soc.*, **164**, A2689 (2017).
8. J. Cannarella and C. B. Arnold, *J. Power Sources*, **245**, 745 (2014).
9. A. G. Hsieh, S. Bhadra, B. J. Hertzberg, P. J. Gjeltema, A. Goy, J. W. Fleischer, and D. A. Steingart, *Energy Environ. Sci.*, **8**, 1569 (2015).
10. C. Bommier, W. Chang, Y. Lu, J. Yeung, G. Davies, R. Mohr, M. Williams, and D. Steingart, *Cell Reports Physical Science*, **1**, 100035 (2020).
11. W. Chang, C. Bommier, T. Fair, J. Yeung, S. Patil, and D. Steingart, *J. Electrochem. Soc.*, **167**, 090503 (2020).
12. W. Chang, R. Mohr, A. Kim, A. Raj, G. Davies, K. Denner, J. H. Park, and D. Steingart, *J. Mater. Chem. A Mater. Energy Sustain.*, **8**, 16624 (2020).
13. W. Chang and D. Steingart, *ACS Energy Lett.*, **6**, 2960 (2021).
14. W. Chang, R. May, M. Wang, G. Thorsteinsson, J. Sakamoto, L. Marbella, and D. Steingart, *Nat. Commun.*, **12**, 6369 (2021).
15. S. Biwa, S. Nakajima, and N. Ohno, *J. Appl. Mech.*, **71**, 508 (2004).
16. R. S. Dwyer-Joyce, B. W. Drinkwater, and A. M. Quinn, *J. Tribol.*, **123**, 8 (2001).
17. B. Drinkwater and P. Cawley, *Ultrasonics*, **35**, 479 (1997).
18. A. Masias, N. Felten, R. Garcia-Mendez, J. Wolfenstine, and J. Sakamoto, *J. Mater. Sci.*, **54**, 2585 (2019).
19. J. L. Allen, S.-D. Han, P. D. Boyle, and W. A. Henderson, *J. Power Sources*, **196**, 9737 (2011).
20. E. R. Logan, A. J. Louli, M. Genovese, S. Trussler, and J. R. Dahn, *J. Electrochem. Soc.*, **168**, 060527 (2021).
21. B. Parimalam and B. Lucht, *J. Electrochem. Soc.*, **165**, 2 (2018).
22. K. L. Harrison et al., *ACS Appl. Mater. Interfaces*, **13**, 31668 (2021).
23. M. Genovese, A. J. Louli, R. Weber, C. Martin, T. Taskovic, and J. R. Dahn, *J. Electrochem. Soc.*, **166**, A3342 (2019).
24. W. Chang, *Electrochem. Soc. Interface*, **30**, 32 (2021).
25. M. W. Verbrugge and B. J. Koch, *J. Electrochem. Soc.*, **141**, 3053 (1994).
26. A. Verma, H. Kawakami, H. Wada, A. Hirowatari, N. Ikeda, Y. Mizuno, T. Kotaka, K. Aotani, Y. Tabuchi, and P. P. Mukherjee, *Cell Reports Physical Science*, **2**, 100301 (2021).